Flux retrieval optimization with a nonscanner along-track broadband radiometer

A. Bodas-Salcedo, J. F. Gimeno-Ferrer, and E. López-Baeza
Unidad de Investigación de Teledetección, Departamento de Termodinámica, Universidad de Valencia, Spain

Received 4 February 2002; revised 7 October 2002; accepted 9 October 2002; published 25 January 2003.

[1] The theoretical behavior of broadband flux retrieval is analyzed with the aid of a radiance field database. Several angular inversion models are developed for different viewing configurations, with special emphasis in a nonscanner along-track design concept. Results show that the performance of these angular models depends on the viewing zenith angle (VZA). When cloud cover is predominant within the observed scene, VZAs around 55° (shortwave) and 50° (longwave) minimize the error when deriving fluxes. These results might help in the design of future missions where the main idea is to obtain accurate instantaneous measurements of top of atmosphere reflected and emitted fluxes. Such measurements can be used as a constraint to derive atmospheric profiles from active instruments (lidar and cloud profiling radar), onboard the same platform. For this purpose, along-track configurations are very good candidates because the flux retrieval can be optimized by using different views of the same pixel almost simultaneously from the same platform. *INDEX TERMS:* 1610 Global Change: Atmosphere (0315, 0325); 1640 Global Change: Remote sensing; 3359 Meteorology and Atmospheric Dynamics: Radiative processes; 3360 Meteorology and Atmospheric Dynamics: Remote sensing; *KEYWORDS:* Earth radiation budget, flux retrieval, angular distribution model

Citation: Bodas-Salcedo, A., J. F. Gimeno-Ferrer, and E. López-Baeza, Flux retrieval optimization with a nonscanner along-track broadband radiometer, *J. Geophys. Res.*, *108*(D2), 4061, doi:10.1029/2002JD002162, 2003.

1. Introduction

[2] The Earth radiation budget (ERB), defined as the ensemble of top of atmosphere (TOA) incoming and outgoing radiation fluxes is what drives the Earth's climate by controlling atmospheric and oceanic thermodynamic engines. In terms of spectral range, the main energy input to the Earth-atmosphere system occurs in the 0.2 to 4 μm region, which is the emission region of the Sun according to its temperature, whereas the Earth emits mainly in the 4 to 200 μm region. Due to their relative position, these two regions are called shortwave (SW) and longwave (LW) bands, respectively. Obviously, both the Sun and the Earth emit radiation at larger wavelengths, although the energy contribution of these regions is small.

[3] ERB has always been a quantity of great interest in climatology [*Hunt et al.*, 1986; *House et al.*, 1986], although it can only be determined accurately enough from space, with the aid of calibrated broadband sensors onboard satellites. The first ERB measurements from satellites were taken with the Explorer 7 satellite, launched in 1959 [*Suomi*, 1961]. These ERB measurements continued in the 1960s using several radiometers onboard the TIROS-series satellites. A second generation of ERB instruments started with the launch of NIMBUS 6 in 1975 and NIMBUS 7 in 1978 [*Jacobowitz et al.*, 1984], which, for the first time, provided information about the ERB at a relatively high spatial resolution. The next step was the successful ERBE mission [*Barkstrom and Smith*, 1986; *Barkstrom et al.*, 1989; *Ramanathan et al.*, 1989], which provided narrow field of view (NFOV) scanner measurements of the ERB from 1985 to 1989, and a 16-year record of nonscanner measurements. After a gap of 5 years in NFOV scanner measurements, the ScaRaB sensor onboard Meteor monitored the ERB from March 1994 to February 1995 [*Kandel et al.*, 1998]. The second flight model of ScaRaB, onboard Resurs, provided sparse ERB data between October 1998 and April 1999 [*Duvel et al.*, 2001]. Presently, CERES instruments [*Wielicki et al.*, 1996, 2002] are taking over the task of providing high-quality measurements of the ERB both globally and on a long-term basis. The first well calibrated broadband radiometer onboard a geostationary platform, the Geostationary Earth Radiation Budget (GERB), launched in August 2002, should provide new insights on the ERB thanks to its high temporal frequency (15 min).

[4] One of the main error sources when measuring the ERB is the lack of knowledge of the anisotropy of the observed scene radiance field. Major efforts have been made over the last 25 years to build and improve angular distribution models (ADMs) that account for this anisotropy, thus allowing us to retrieve flux measurements with the desired accuracy. *Davies* [1984] showed that viewing geometry influences the accuracy of retrieval, and that the optimum region for viewing zenith angles (VZAs) is around 60°.

[5] Our main interest in this paper is to present a study of the behavior of different angular inversion models with respect to the observing geometry, with the purpose of

0148-0227/03/2002JD002162$09.00

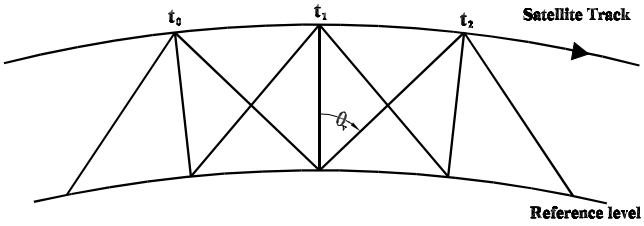

Figure 1. Diagram of the along-track configuration.

selecting an a priori optimum configuration for an along-track NFOV broadband radiometer, based on theoretical simulations carried out with a radiative transfer code. These results will help in the design of future missions, like European Space Agency (ESA) Earth Clouds, Aerosols, and Radiation Explorer (EarthCARE) [*ESA*, 2001], where the main idea is not to monitor the TOA ERB on a global scale, but to obtain accurate instantaneous TOA ERB measurements as a constraint to derive atmospheric profiles from active instruments (lidar and cloud profiling radar), onboard the same platform. For this purpose, along-track configurations are very good candidates because the flux retrieval can be optimized by using different views of the same pixel from the same platform. Figure 1 shows a diagram of an along-track observing configuration with three fixed views, one nadir, and two symmetric off-nadir views. This allows us to obtain three views of the same target at almost the same time. Other along-track configurations with a dense angular sampling will be studied, but this paper will focus especially on the configuration shown in Figure 1, with only three views. This latter configuration was finally implemented in pre-phase A EarthCARE optimization studies.

[6] When using along-track measurements, several issues regarding the geometry need to be discussed. First, with a NFOV scanner like ERBE, ScaRaB or CERES, the pixel size changes when increasing the VZA. This is an additional error source if several along-track measurements of the same geographical position are used, because the off-nadir pixels are not seeing the same area as the nadir. As we shall focus on nonscanner along-track measurements (Figure 1), pixel size can be kept constant by using a different telescope for each view, and therefore that additional error can be reduced significantly with this configuration.

[7] Secondly, the reference level where all the along-track measurements are collocated must correspond to the level where the reflection takes place. For instance, if clouds are present, the reference level corresponds to the cloud top, whereas under clear sky the main reflection comes from the surface layer. One possible approach to overcome this problem would be to have a large overlap between consecutive pixels, so that the off-nadir measurements are selected based on the actual main reflection level for that particular scene.

[8] Although these two problems are conceptually different, both of them cause similar effects: changes in the scenes observed by nadir and off-nadir views. These issues must be taken into account when constructing ADM models from satellite data, although they are not considered here.

[9] Another general issue concerning along-track measurements is the spatial coverage. Along-track data typically have many gaps between measurements and, therefore, have worse spatial sampling than cross-track measurements, which becomes an error source when computing regional means. However, since our interest is flux retrieval on an instantaneous pixel basis as a constraint of atmospheric profiles, the spatial coverage is not a problem, and will not be considered here.

[10] Although the study was carried out for different representative surfaces, the results analyzed here mainly correspond to those obtained for ocean. The reason is that results over ocean represent the worst case, and the main conclusions do not change significantly for the rest of surfaces. In addition, our main interest is to study the inversion process under mostly cloudy or overcast conditions, where the main signal comes from the cloud layer and not from the surface.

[11] Section 2 states the problem of obtaining flux measurements from NFOV radiometers onboard satellites. The study has been carried out with the aid of a database presented in section 3. Section 4 shows the results obtained for the flux retrieval behavior by using a single-view methodology. Section 5 explains the methodology developed and shows the results obtained for an along-track NFOV radiometer, which allows a multiple-view approach. The results are summarized, and conclusions are drawn in section 6.

2. Inversion Process

[12] Given a radiance field $L(\theta, \theta_v, \phi)$ at the TOA, where θ is the solar zenith angle (SZA), θ_v the satellite viewing zenith angle, and ϕ the relative azimuth between the satellite and the Sun, the flux leaving the Earth-atmosphere system is obtained by integration over the solid angle ω of the upper hemisphere:

$$F(\theta) = \int_{\Omega} L(\theta, \theta_v, \phi) \cos\theta_v d\omega. \quad (1)$$

[13] Figure 2 shows the convention used for the observing geometry. Relative azimuth ranges only from 0 to 90, in which the origin is the principal plane. The radiance field is assumed to be symmetric with respect to this plane. In order to distinguish between forward and backward scattering half-sides, negative VZAs are used for the latter. This notation takes advantage of the along-track concept we shall study in section 5.

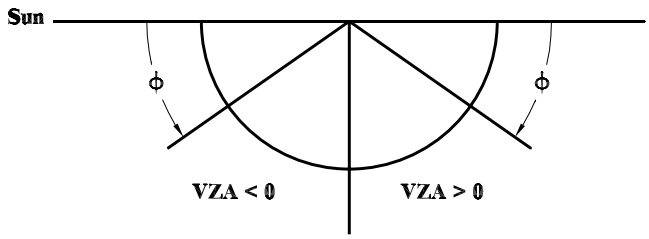

Figure 2. Plan view of the observing geometry. Relative azimuth, ϕ, ranges from 0° to 90° with respect to the principal plane. Positive VZAs are in the forward scattering half-side, whereas negative ones correspond to the backward scattering half-side.

[14] NFOV radiometers measure flux in a small solid angle in specific directions. Since not all directions can be measured, an inversion procedure has to be used to estimate the exiting flux from the Earth-atmosphere system. This inversion procedure can be based on an ADM that takes the mean behavior of the anisotropy of the radiance field into account, in order to allow for flux retrieval from a single radiance measurement.

[15] Although in this study we will only focus on the radiance to flux inversion, the full inversion process is more complex and contains several steps, each of which is a source of error. Previously to the radiance to flux inversion, calibration, unfiltering, and scene identification have to be carried out [*Smith et al.*, 1986; *Lee et al.*, 1998; *Loeb et al.*, 2001]. We shall assume perfect calibration, perfect scene identification, and perfect unfiltering.

[16] First efforts to develop angular models were done by *Raschke et al.* [1973], by using NIMBUS 3 measurements and empirical models of the anisotropy of three scenes, namely ocean, snow, and a cloud-land combination. Later on, *Jacobowitz et al.* [1984] used four scenes (ocean, land, snow-ice, and cloud) for NIMBUS 7 Earth Radiation Budget (ERB) data, with angular models derived by *Taylor and Stowe* [1984] from ERB scanner observations. ERBE included angular distribution models in its inversion algorithms [*Smith et al.*, 1986], with 12 scenes, which are widely described by *Suttles et al.* [1988, 1989].

[17] Although we use the same general scheme for ADMs as in ERBE, ADMs from satellite data result from data sets that contain, in principle, representative samples of the subscenes for each scene type. A subscene is a set of cloud, atmospheric and aerosol parameters that influence the anisotropy of the radiance field and are not included in the scene definition. However, satellite data provide intrinsically incomplete samples in the angular space, with scene identification usually relying on narrowband data for the same observed scenes. In addition to the intrinsic errors of the inversion procedure, another error source in the inversion procedure is scene misclassification [*Smith and Manalo-Smith*, 1995]. In our case, the simulations provided a perfect angular sampling, and we also assumed a perfect scene identification. Therefore, errors due to scene misclassification were not considered here. A more complete investigation would involve applying a scene identification procedure to the simulated radiances, and not assuming that it would always yield the scene class that went into the simulation.

[18] In this study, we have worked with a scene definition in terms of surface type and cloud cover. Six ranges of cloud cover, C, and three surface types were considered. These scenes are presented in Table 1, where the angular bins are also shown. Additional parameters also influence the anisotropy of Earth scenes (cloud optical depth, cloud phase, etc.). Their inclusion in the scene definition will always reduce the retrieval error, but in this study they are only used as variable parameters to generate subscenes. Our aim was to focus on the root mean square error (RMSE) dependence with the observing geometry, and on the study of specific methodologies for along-track radiometers. That is the reason why the scene definition was kept as simple as possible. To build the angular models, all combinations of surface type and cloud cover for any observing geometry were considered because we were looking for an optimal angle consideration. In section 5, the dependence with VZA is removed when working with an extended ADM definition that uses the along-track configuration.

Table 1. Scene Definitions for the Present Study[a]

Parameter	Interval
θ	[0–25, 25–35, 35–45, 45–55, 55–65, 65–70]
θ_v	5° interval
ϕ	[0–10, 10–30, 30–60, 60–90]
Surface	ocean, vegetation, desert
Cloud cover (C_l) (%)	[0–1, 1–25, 25–50, 50–75, 75–99, 99–100]

[a] C_l is the cloud cover, while l is the subscript that identifies the interval (C_1 is clear-sky, and C_6 is overcast).

[19] Once the scene definition has been made, the next step is to build the ADM. For each surface type, simulations with a radiative transfer code provided a set of radiances and fluxes, $[L^m_{ijkl}, F^m_{ijkl}]$, where the subscripts i, j, k, l correspond to intervals in SZA, VZA, ϕ, and C, respectively, and the superscript m denotes a particular radiance in that bin. The flux, F^m_{ijkl}, was obtained by direct integration of the radiances L^m_{ijkl} over the viewing angles, VZA and ϕ. It should be noted that although the flux only depends on SZA and C, the j and k indexes have been kept, because in the inversion process there will be a separate flux estimate for each radiance.

[20] With these radiances and fluxes, the anisotropic factor, R, is computed for each bin as

$$R_{ijkl} = \frac{\pi \bar{L}_{ijkl}}{\bar{F}_{ijkl}}, \tag{2}$$

where the overbar means average over all the values in the $ijkl$ bin. This averaging procedure was done over all the radiances of each subscene. Constant weighting was applied to those sub-scene radiances for a given scene type into the viewing angle bins.

[21] Once the ADMs for every scene type were built, a flux estimate, $\hat{F}^m_{ijkl}$, was obtained from direct application of equation (2), by means of the radiance and the corresponding anisotropic factor

$$\hat{F}^m_{ijkl} = \frac{\pi L^m_{ijkl}}{R_{ijkl}}. \tag{3}$$

[22] Given the possibility of computing the radiance field with the aid of a radiative transfer code, and therefore the flux, for many different scenes, we studied the performance of the retrieval algorithm by means of the RMSE,

$$RMSE_{ijkl} = \left[\frac{1}{N_{ijkl}} \sum_{m=1}^{N_{ijkl}} \left(\hat{F}^m_{ijkl} - F^m_{ijkl} \right)^2 \right]^{1/2}, \tag{4}$$

which compares the actual flux, given by the code, F^m_{ijkl}, and the estimated flux from the inversion process, $\hat{F}^m_{ijkl}$. Since VZA can be selected a priori with a sensor in along-track configuration, we shall focus our attention on the parameterization of the RMSE with respect to VZA.

[23] In summary, for each angular combination, there is an average radiance made from all subscenes, from which

an anisotropic factor is derived using an average flux by means of equation (2). Then, using these anisotropic factors, new fluxes are calculated for each angular combination as in equation (3). The estimated fluxes, $\hat{F}^m_{ijkl}$, are compared to those considered correct, F^m_{ijkl}. Then, the optimal viewing angle is sought by finding where the RMSE is minimized.

3. Database

[24] In order to build the anisotropic models as previously explained, a radiance field database in a wide range of atmospheric conditions had to be developed. This database provided the exiting radiance field at TOA, both in SW and LW bands. The database was built using the plane-parallel radiative transfer code Streamer 2.5p [*Key*, 1998], because it can compute radiances and fluxes for a wide variety of clear and cloudy conditions. It uses a discrete ordinates solver [*Stamnes et al.*, 1988] for radiance computations in different viewing geometries. Four streams with the correction in radiances of *Nakajima and Tanaka* [1988] were used in radiance computations, and TOA fluxes ($\bar{F}_{ijkl}$) were obtained by computing the hemispherical integral (equation (1)) from these radiances.

[25] In order to justify the low number of streams used to compute radiances in SW, a sensitivity study was carried out with two clouds over ocean with optical depth, τ, of 1 and 20. Results from four-stream computations were compared with 16-stream computations, the latter being much more accurate but also 4 times more expensive in computation time. Radiances for the $\tau = 20$ case are more accurate in relative terms, and less accurate in absolute values because of the larger amount of energy reflected. For $\tau = 1$, fluxes generally agree within 3%, and always within 5%. The mean bias for all SZAs used was -1.4%. For radiances, 50% of them agree within 2%, and 80% within 5%. For $\tau = 20$, fluxes generally agree within 0.6%, and always within 1.3%. The mean bias for all SZAs used was -0.1%. For radiances, 75% of them agree within 2%, and 99% within 5%. In both cases, more than 99% of the radiances agree within 10% with respect to the 16-stream results. Summarizing, most of the radiances are in a $\pm 5\%$ interval with respect to the 16-stream computations, which is a reasonable accuracy for the purpose of the study.

[26] Only four gases are present in Streamer, H_2O, CO_2, O_2, and O_3, and absorption amounts are determined with the exponential-sum fitting of transmissions technique [*Wiscombe and Evans*, 1977]. The built-in surface albedo models in Streamer are lambertian. Spectral albedo data for sand and vegetation are taken from *Tanré et al.* [1986], and sea data are based on *Briegleb et al.* [1986]. The ocean albedo model depends on SZA, and is not spectrally dependent, while the vegetation and sand models are spectrally dependent but independent of SZA. In Streamer, cloud optical properties are based on parameterization schemes from three different sources. For water clouds, data are taken from *Hu and Stamnes* [1993]. For ice clouds in SW, the six-band parameterization of *Fu and Liou* [1993], based on randomly oriented hexagonal crystals, is used. Longwave ice cloud optical properties are based on Mie calculations using spherical particles for 132 wavelengths. Aerosol models are based on the optical properties given by *Shettle and Fenn* [1979].

Table 2. Database Description, Showing the Values of the Parameters Varied to Build the Radiance Database[a]

Parameters	Values
	SW Clear Sky
Surface	ocean, desert, vegetation
SZA	0–70°, 5° intervals
Atmosphere	TRO, MLS, MLW, SAS, SAW
WV factor	0.6, 0.8, 1.0, 1.2, 1.4
Aerosols	maritime, rural, tropospheric, (high and low visibility)
	SW Cloudy Sky
Surface	ocean, vegetation, desert
SZA	0–70°, 5° intervals
Atmosphere	TRO, MLS, MLW, SAS, SAW
Cloud	low, middle, high
τ	0.1, 0.3, 1, 3, 10, 30
Aerosols	maritime, rural, tropospheric, (high visibility)
	LW Clear Sky
Surface emittance	1
Surface T(K)	$T_0 - 10$, $T_0 - 5$, T_0, $T_0 + 5$, $T_0 + 10$
Atmosphere	TRO, MLS, MLW, SAS, SAW
WV factor	0.6, 0.8, 1.0, 1.2, 1.4
Aerosols	maritime, rural, tropospheric, (high and low visibility)
	LW Cloudy Sky
Surface T(K)	$T_0 - 10$, $T_0 - 5$, T_0, $T_0 + 5$, $T_0 + 10$
Atmosphere	TRO, MLS, MLW, SAS, SAW
Cloud	low, middle, high
τ	0.1, 0.3, 1, 3, 10, 30
Aerosols	maritime, rural, tropospheric, (high visibility)

[a]A total of 7860 radiance fields were obtained, 5760 for SW, and 2100 for LW. WV factor is a scaling factor that applies to the water vapor amount of the standard profiles. T_0 is the surface temperature of the standard atmosphere. Acronyms for standard atmospheres are TRO, tropical; MLS, midlatitude summer; MLW, midlatitude winter, SAS, subartic summer; SAW, subartic winter.

[27] Many parameters can be modified, but not all of them have the same impact on the radiance field anisotropy. Therefore, we mainly focused on those that change the radiance field significantly. These parameters, and the range in which they vary, were selected by band (SW, LW), and by cloudiness (clear, cloudy). Table 2 shows the parameters which were modified to build the database. They were organized in four groups; SW and LW bands, and clear sky and cloudy conditions, respectively. Partly cloudy conditions were obtained as linear combination of clear and cloudy radiances.

[28] When designing the database, due to the fact that Streamer computes SW and LW radiances independently, special efforts were made to ensure that the four database subsets (SW clear sky, SW cloudy sky, LW clear sky, LW cloudy sky) were compatible, by varying the common parameters in the same range. That means that each SW radiance field has its LW counterpart. For example, although aerosols only really influence SW clear-sky radiance field anisotropy, they were also varied in LW. Due to the fact that computations took a huge amount of CPU time, we considered the compatibility between SW and LW bands to be crucial in order to make the database as general as possible. For clear sky, the nongeometric parameters that were varied are precipitable water content, type of standard atmosphere, type of surface and aerosols in the SW region of the spectrum, and precipitable water content, type of standard atmosphere, aerosols, and surface temperature in the LW region.

Table 3. Cloud Top Height (k)

Atmosphere	Low Cloud	Middle Cloud	High Cloud
TRO	2	6	14
MLS, MLW	2	5	12, 10
SAS, SAW	2	5	10, 8
ARS, ARW	2	4	8

[29] The main strength of the work carried out when developing this database was done for cloudy sky conditions, which represent the most difficult conditions for the flux retrieval procedure. Three cloud layers were introduced, ranging in visible optical depth from 0.1 to 30. The mean cloud optical depth is 7.4, which seems to be a reasonable value as compared to those of the International Satellite Cloud Climatology Project (ISCCP) [*Rossow and Schiffer*, 1991, 1999]. The global mean cloud optical depth reported by *Rossow and Schiffer* [1991] from July 1983 to June 1986 is 9, and with a later ISCCP data set (1986–1993) and an improved analysis method, the mean cloud optical depth is 3.9 [*Rossow and Schiffer*, 1999]. The latter value is not a linear average, being smaller than the corresponding linear average. The lower and middle layers contained a water cloud, whereas the upper layer was comprised of ice crystals. These clouds were allocated over different surfaces in the case of the SW band, and over black surfaces with different temperatures in LW. Table 3 shows that the cloud top height of these three cloud layers was selected according to the standard atmosphere used. It was higher for the tropics, and descended poleward.

[30] As we have already mentioned regarding the statistics used in the construction of the ADMs, equal probability assumption of all the subscenes was applied. That means that each subscene in the range considered for cloud cover and SZA, subscripts l and i, respectively, had the same weight when the ADMs were constructed on the basis of the computed radiance fields in all outgoing directions j, and k. In addition, the same weight was applied when evaluating the RMSE. The RMSE may be overestimated if one subscene dominates the statistics in reality, but our main purpose is to study the variability of the RMSE with the observing geometry, rather than obtaining accurate absolute values of the inversion error, for which detailed statistics are needed.

[31] Although for the purpose of this study, only broadband radiances were needed, narrowband radiances were computed at Streamer resolution, that is, 24 channels in the SW region and 105 in the LW. These radiances were obtained for every 5° intervals in relative azimuth, and 0.01 intervals in cos θ_v. Broadband radiances were obtained by adding the narrowband ones.

4. Single-View Methodology

[32] In this section, we will follow the procedure explained in section 2 to build angular distribution models from the radiance database, and study their behavior with respect to viewing geometry. The inversion methodology that we are going to study is the methodology used for past and present scanners such as ERB, ScaRaB, and CERES, which can be applied to all instrument observing modes (across-track, along-track, etc.). This is possible by the fact that with this methodology, only a single radiance is needed to obtain a flux estimate by using equation (3).

4.1. SW Band

[33] As has been commented above, in an along-track configuration, VZA can be freely selected for every pixel. This allows to optimize the flux retrieval error by studying the RMSE with respect to VZA. Figures 3 and 4 show the RMSE of the SW flux retrieval over ocean as a function of VZA, for the two extreme cases, clear sky and overcast. Each figure has four plots to distinguish between ϕ intervals, and the different curves within each plot correspond to different SZA intervals. In terms of cloud cover, it is clearly appreciated that the retrieval error increases with cloud cover, and a pattern of its behavior with respect to VZA also appears. This pattern shows two preferred regions, in the 50°–60° regions, both in forward and backward scattering directions. This behavior only appears when the radiance field is dominated by the presence of clouds in the scene (Figure 4). For clear sky (Figure 3) or small cloud cover, the behavior with respect to VZA does not show any common pattern for different SZA and ϕ intervals, although in those cases the absolute error is much smaller. For overcast conditions (Figure 4), the variability in the RMSE caused by changes in SZA is smaller than that caused by changes in VZA.

[34] Table 4 presents the mean SW fluxes, $\bar{F}_{ijkl}$, for each surface type. Relative root mean square errors in the flux retrieval with respect to these mean SW fluxes range from 3 to 9%, if VZA is close to −55°, and from 12 to 23% at nadir viewing. As seen in Figure 4, the main impact of SZA is the change of the positions of the two local minima, which do not remain constant when varying SZA. The same conclusions as for the behavior with respect to SZA can be held in the case of variation of ϕ, although in this case, as the SW flux does not depend on ϕ, relative errors have the same shape.

[35] It must be noted that the mean SW fluxes for clear ocean in Table 4 increase slightly with SZA, which do not

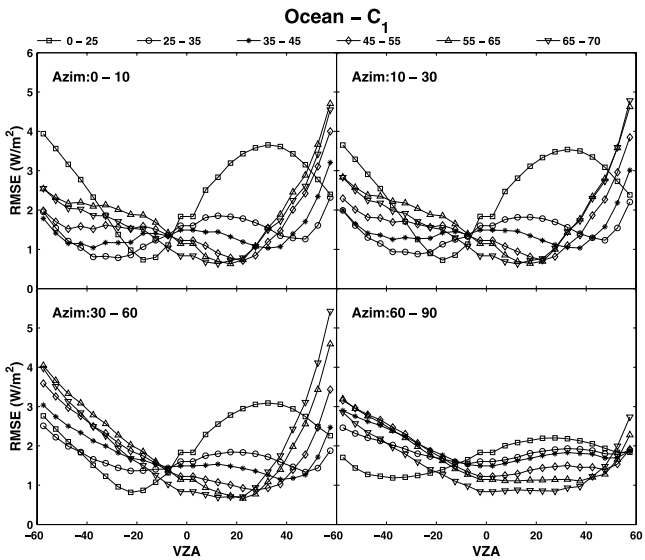

Figure 3. Shortwave flux retrieval algorithm RMSE under clear-sky conditions over ocean as a function of VZA for different SZA and ϕ. The legend shows SZA intervals.

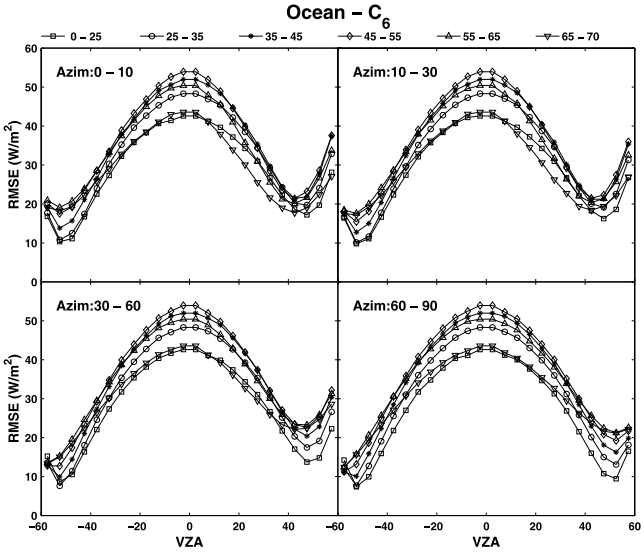

Figure 4. Same as Figure 3, but for overcast sky.

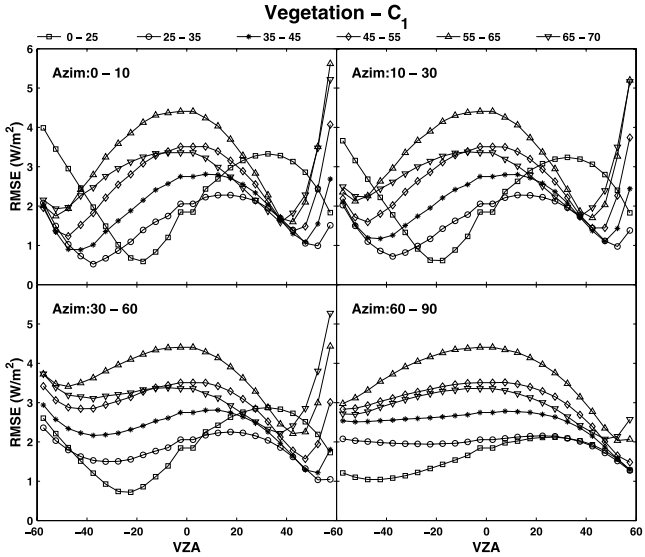

Figure 5. Shortwave flux retrieval algorithm RMSE under clear-sky conditions over vegetation as a function of VZA for different SZA and ϕ.

agree with the results of *Suttles et al.* [1988]. This may be caused by the ocean albedo model for the direct radiation used in Streamer. This albedo model [*Briegleb et al.*, 1986] accounts for the Fresnel reflection and the backscattering from the bulk ocean, and its dependence with the SZA explains the increase of mean SW fluxes obtained for clear ocean.

[36] Whereas Figures 3 and 4 show the results obtained over ocean, Figures 5 and 6 show analogous results, but for vegetated land. The differences between clear ocean and vegetated surfaces come from two sources. First, the surface albedo models, which differ both in magnitude and in directional response. The ocean albedo model used in Streamer strongly depends on SZA, whereas the vegetation model does not depend on SZA. Second, the aerosol models used were different, a maritime model over ocean, and a tropospheric model over vegetation. These aerosol models have different optical properties which influence the anisotropy of the radiance field, and therefore the retrieval error. Due to the fact that surface albedo models are lambertian, these figures do not take into account the impact of the bidirectional response of the surface. Thus, different behavior under highly anisotropic real scenes, like clear sky ocean in forward and backward scattering directions, should be expected. Different behavior for overcast ocean and vegetation may also be caused by the different surface models under optically thin clouds. The ocean has the lowest albedo, and even for overcast sky, if the overlying cloud has a very small optical depth, the reflected SW flux will be small. On the other hand, with optically thick clouds, the reflected SW flux will be similar over ocean and land. This introduces a greater variability over ocean, which increases

Table 4. Mean TOA SW Fluxes for Each Cloud Cover and SZA Intervals for Ocean, Vegetation, and Desert[a]

	Mean TOA SW Flux					
Cloud Cover	0–25	25–35	35–45	45–55	55–65	65–70
			Ocean			
C_1	86	84	85	88	91	92
C_2	116	113	112	112	110	106
C_3	175	170	165	158	147	133
C_4	236	228	219	205	184	162
C_5	295	285	272	252	221	189
C_6	325	314	299	275	239	203
			Vegetation			
C_1	330	300	270	234	191	155
C_2	347	317	287	250	204	166
C_3	381	351	320	280	231	187
C_4	415	386	354	312	258	210
C_5	449	419	387	343	284	231
C_6	466	437	404	358	298	242
			Desert			
C_1	271	248	224	195	161	132
C_2	290	267	243	213	176	144
C_3	328	304	279	246	205	168
C_4	366	342	317	281	234	193
C_5	404	380	353	315	264	216
C_6	423	399	371	332	278	229

[a]Units are W/m^2.

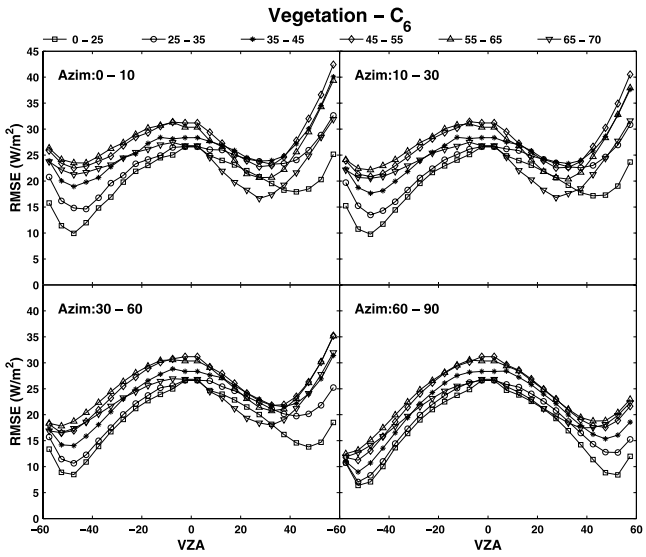

Figure 6. Same as Figure 5, but for overcast sky.

the RMSE. The results over desert are not shown here, although its behavior is similar and all the previous comments can be directly applied to desert surfaces.

[37] The selection of the VZA which minimizes the RMSE is not clear just from an analysis of the previous figures. However, the best range of VZA for this ADM definition can be established. Figure 7 shows frequency of occurrence histograms of the VZA interval that minimizes the error, for each surface type, and without distinguishing the surface type. In this figure, all cloud cover intervals are included. It shows that the best VZA angle configuration occurs around $-50°$, in the backward scattering direction, when the RMSEs are in the interval range from 5 to 15 W/m^2.

4.2. LW Band

[38] In the longwave part of the spectrum, the anisotropy of the radiance field is smaller than in the shortwave one [*Suttles et al.*, 1988], so a lower radiance to flux inversion error should be expected. By taking this into account, if the angle that minimizes the error for longwave is close to that of the previously selected in the SW study, the election of the best inversion angle for both bands simultaneously should be based mainly on the SW study results. The same steps that were followed in SW have been used to investigate the behavior of the flux retrieval error in LW. Although *Minnis and Khaiyer* [2000] have shown that there can be strong dependence on relative azimuth over land scenes in the LW radiance field, the radiative transfer code assumes no dependence with SZA and ϕ. Therefore, this issue cannot be addressed with our theoretical computations.

[39] Figure 8 shows the behavior of the longwave RMSE with respect to VZA over ocean. Only positive VZAs are shown due to the axial symmetry explained above. The mean outgoing LW fluxes for the scenes taken into account are, in W/m^2, 256, 251, 243, 234, 225, and 220, in increasing order of cloud cover. That means that, even in the worst case, the error is always lower than 3% with respect to the mean LW flux. As in the shortwave region, the error can be minimized by selecting an appropriate VZA, which for longwave is in

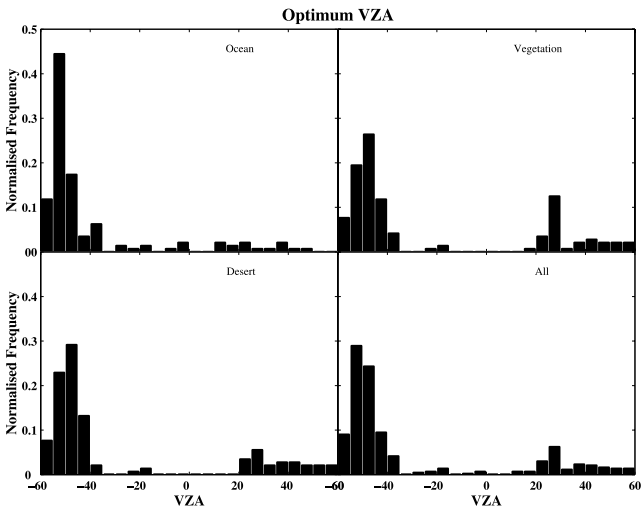

Figure 7. Normalized frequency of occurrence histograms of the VZA that minimizes the error for different surface types (ocean, vegetation and desert), without distinguishing the surface type. All cloud cover intervals are included.

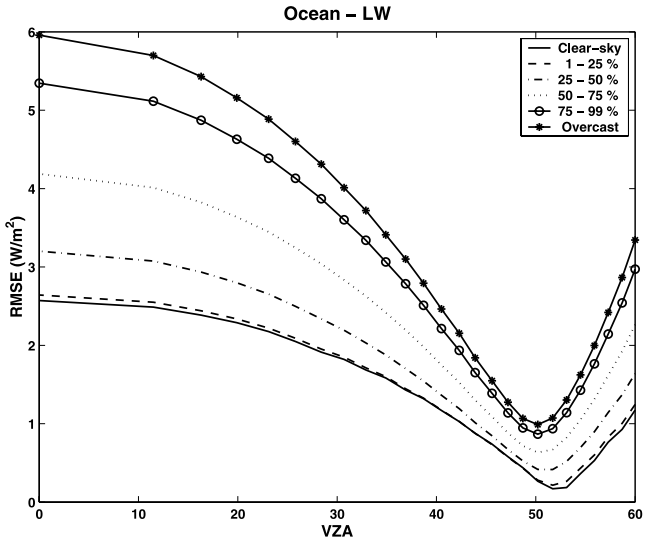

Figure 8. RMSE of the LW inversion as a function of VZA over ocean for different cloud covers. It shows that the lowest error is around 50°.

the region between 45° and 55°. As we can see in this figure, the optimum inversion angle changes slightly with cloud cover, from 52° in clear-sky to 50° in overcast, where the limb-darkening models show a small variability among different scenes [*Smith et al.*, 1994].

5. Methodology for Along-Track Configuration

[40] In the previous section, the study was carried out by using only a single radiance in the inversion procedure. In this section, our purpose is to extend that study by focusing on the radiance to flux inversion with an along-track configuration.

[41] With an along-track observing configuration, there are several available radiances of the same scene at almost the same time, so we can extend the ADM definition and use this new information to estimate the flux with better accuracy. Let us write the definition of the anisotropic factor as

$$R_{ijkl} = \frac{\pi \bar{\mathcal{L}}_{ijkl}}{\bar{F}_{ijkl}}, \tag{5}$$

where we have introduced $\mathcal{L}$ as an "extended radiance." $\mathcal{L}$ may be defined in different ways by using an along-track configuration to look at the same pixel from more than one angle. Similarly to equation (3), the flux will be estimated as

$$\hat{F}^m_{ijkl} = \frac{\pi \mathcal{L}^m_{ijkl}}{R_{ijkl}}. \tag{6}$$

[42] We have studied different methods of defining $\mathcal{L}_n$, where the subscript n is the method label from 1 to 6:

$$\mathcal{L}_1(\theta, \theta_v, \phi, C) = N_1(\theta, C) L(\theta, \theta_v, \phi, C). \tag{7}$$

$$\mathcal{L}_2(\theta, \phi, C) = N_2(\theta, C) \int_{-\theta_v^{max}}^{\theta_v^{max}} L(\theta, \theta_v, \phi, C) |\sin\theta_v| \cos\theta_v d\theta_v. \tag{8}$$

$$\mathcal{L}_3(\theta, \phi, C) = N_3(\theta, C) \int_{-\pi/2}^{\pi/2} \hat{L}(\theta, \theta_v, \phi, C) |\sin\theta_v| \cos\theta_v d\theta_v. \tag{9}$$

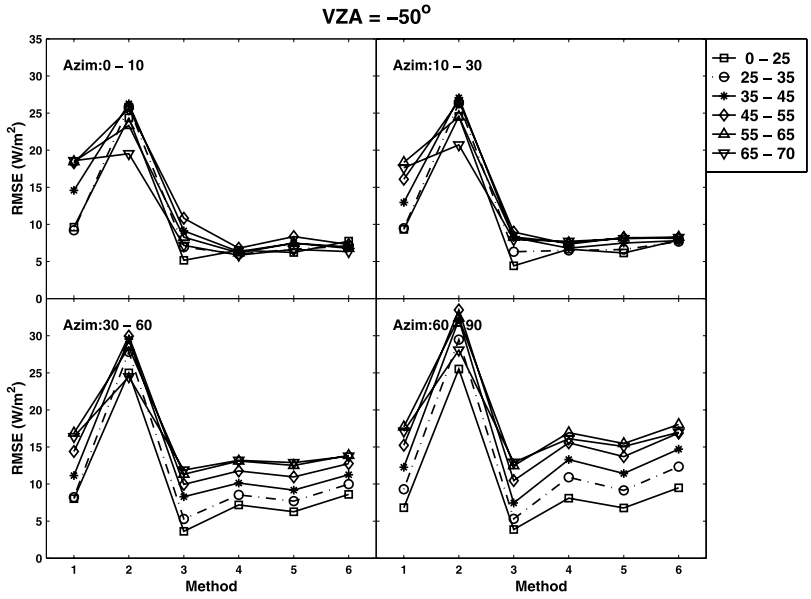

Figure 9. RMSE as a function of the methodology used to build the ADM, for overcast ocean and VZA = $-50°$ ($\pm 50°$ for methods 2 to 6). The method number corresponds to the equation number that defines this method, and the legend shows the corresponding SZA intervals.

$$\mathcal{L}_4(\theta, \phi, C) = N_4(\theta, C) \int_{-1}^{1} \hat{L}(\theta, \cos\alpha_v, \phi, C)|\cos\alpha_v| d(\cos\alpha_v). \tag{10}$$

$$\mathcal{L}_5(\theta, \phi, C) = \text{Same as method 3 but with three viewing angles.} \tag{11}$$

$$\mathcal{L}_6(\theta, \phi, C) = \text{Same as method 4 but with three viewing angles.} \tag{12}$$

[43] Method 1 is the method previously studied, and method 2 is defined as the line integral of the radiances, by assuming continuous scanning. In methods 3 and 4, $\hat{L}$ is a polynomial fitting of the along-track radiances, respectively, as a function of VZA or cos α_v, where α_v is the elevation viewing angle (from 0° to 180°). Methods 5 and 6 are similar to 3 and 4, respectively, but using only three measurements instead of a dense sampling, which is the simplest symmetric configuration in along-track observation. For along-track methodologies, the anisotropic factor does not depend on VZA because of the integral in the definition of $\mathcal{L}$. $N_n(\theta, C)$ are the normalization factors so that the following normalization conditions are obtained:

$$2\int_0^{\pi/2} d\phi \int_{-\pi/2}^{\pi/2} R_1(\theta, \theta_v, \phi, C)\cos\theta_v|\sin\theta_v| d\theta_v = \pi \tag{13}$$

$$2\int_0^{\pi/2} R_n(\theta, \phi, C) d\phi = \pi, n = 2, \ldots, 6. \tag{14}$$

[44] The factor of 2 in equations (13) and (14) is added because the radiance field is symmetric with respect to the principal plane, so there is only half integration. By using equations (1) and (2), it is easy to see that $N_1(\theta, C) = 1$. The rest of the normalization factors are not equal to unity, and depend on SZA and C. In fact, the selection of the normalization condition is somewhat arbitrary if it is taken into account in the definition of $\mathcal{L}_n$, by adding a normalization factor which preserves the mean flux and, therefore, the energy.

[45] When a dense angular sampling is used, as in methods 3 and 4, the order of the polynomial fitting is 4, and if only three along-track radiances are used, as in methods 5 and 6, the polynomial order is 2 to avoid overfitting. Due to the fact that surface albedo models used in the radiative transfer model are lambertian, the strong forward scattering peak for clear ocean is not well represented in the simulated radiance fields, and the error of the polynomial fitting with only three terms is not increased in those cases. However, with more realistic radiance fields for clear ocean near the principal plane, the second-order fitting is not expected to be accurate.

5.1. SW Band

[46] First, the impact of the method used on the retrieval error was studied, and Figures 9 and 10 show the comparison for two VZA, $-50°$ and $-60°$, respectively. For methods 2 to 6, which use more than a single radiance, angles in the along-track plane to maxima VZA of $\pm 50°$ and $\pm 60°$ were considered.

[47] The main reason for the poor behavior of method 2 is the lack of proportionality in the $F-\mathcal{L}_2$ relationship. Although in methods 2 to 6, multiple radiances are used, they are integrated and converted to only one single value so that equation (5) can be applied. This linearity fails in method 2, reducing the performance of that method. This is a general weakness of ADM models, because the assumption of proportionality between flux and radiance is not always held.

[48] Methods 3 to 6 with VZA = $\pm 60°$ gave smaller RMSEs, while method 4 was the most stable with respect to relative azimuth variations. In the following, we will focus our attention only on method 6, which is analogous to method 4, but using only three views, namely nadir, and the

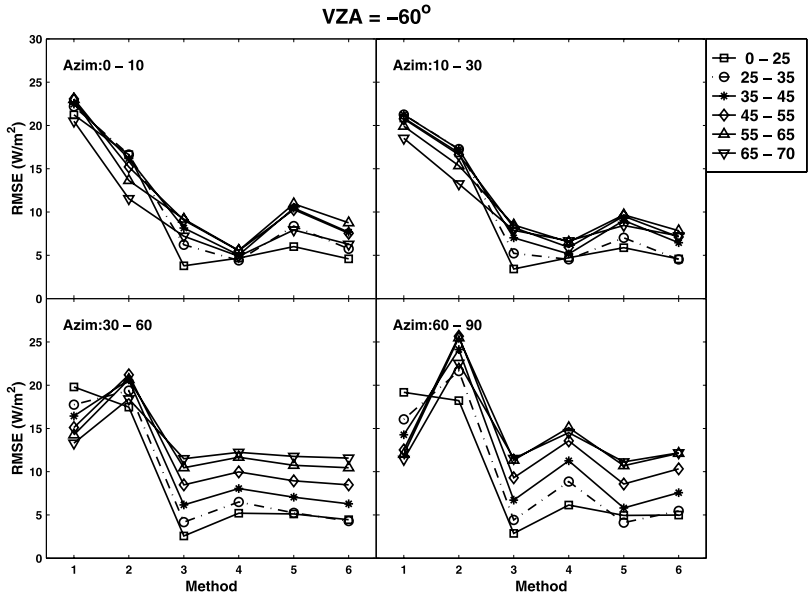

Figure 10. Same as Figure 9, but for VZA = $-60°$ ($\pm 60°$ for methods 2 to 6).

two symmetric off-nadir views. Although continuous angular sampling can be studied from a theoretical point of view, it does not seem to be an option for a real sensor if continuous along-track spatial coverage is needed.

[49] To study method 6 in greater detail, we first selected the VZA for the off-nadir views that minimizes the RMSE. The RMSE for each [*SZA*, ϕ, *C*] bin over ocean was calculated for several VZAs. The VZAs selected were $\pm 45°$, $\pm 50°$, $\pm 55°$, and $\pm 60°$. Figure 11 represents two frequency histograms of the percentage of bins with RMSE greater than a given threshold of 7 W/m^2, as a function of VZA for these four cases. The value selected for this threshold is arbitrary, although it has to be small in order to distinguish the behavior at different VZAs. The left-hand plot takes all the angular bins into account, whereas the right-hand one only considers those compatible with a typical sunsynchronous orbit with equator crossing time at 1300 LST in the descending node. This introduces a constraint between SZA and ϕ which means not all the angular bins are sampled. As we can see, viewing zenith angles of ± 55 and $\pm 60°$ provide smaller errors, while the behavior around $\pm 55°$ is better in the case of the orbit selected. Similar computations have been carried out with a 1030 LST equatorial crossing time, and the error increases. The reason for this increase in error is that bins with larger SZA and ϕ are sampled in the 1030 LST orbit, and these bins usually have larger errors, as we shall see below (Figures 12–14). For a VZA of $\pm 55°$, around 25% of the bins have RMSE greater than 7 W/m^2, and 95% less than 10 W/m^2. In this case, a VZA of $\pm 60°$ is slightly better than $\pm 55°$. As a result, an angle close to $\pm 55° - 60°$ (or even a few degrees greater) seems to optimize the SW flux retrieval algorithm, even using different methodologies to define $\mathcal{L}$ such as those of methods 1 to 6. Hereinafter, we will focus our discussion only on method 6 with off-nadir views at VZA of $\pm 55°$.

[50] Figures 12–14 show the behavior of the RMSE for method 6 and VZA = $\pm 55°$. The *x* axis is now SZA, because there is no dependence in VZA. Results are shown for ocean, vegetation, and desert surfaces, respectively, and each figure presents six plots, each one corresponding to a different cloud cover interval. Different lines distinguish between relative azimuth intervals, as stated in the legend. We can see that the largest errors are reached over ocean, as in the single-view study. In any case, these three figures share common patterns, showing that the error increases with cloud cover, and solar zenith angles up to $\pm 50°$ or $\pm 60°$. Except for ocean, different behavior with respect to relative azimuth is appreciated only at large solar zenith angles. Generally, the RMSE of each bin is below 10 W/m^2. Figures 12–14 show the RMSEs for all the [SZA, ϕ] combinations. When a particular orbit is selected, some of these [SZA, ϕ] pairs may never occur, as it happens in the case of those with RMSE greater than 7 W/m^2 for the 1300 LST orbit. That means that the mean error computed by

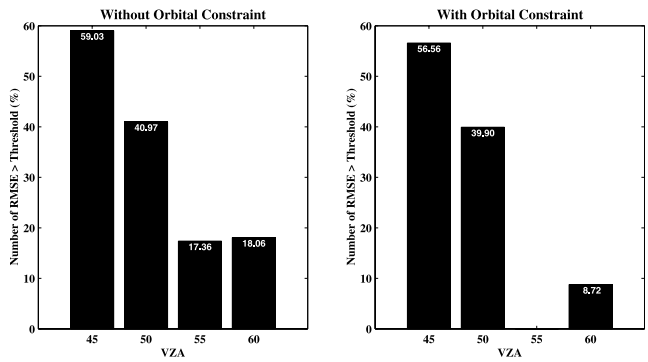

Figure 11. Percentage of cases with RMSE greater than 7 W/m^2 for method 6 for different VZA configurations. Computations were made over ocean surface. The left-hand side plot corresponds to results without orbital constraint, and the right-hand plot was obtained taking a specific orbital constraint into account.

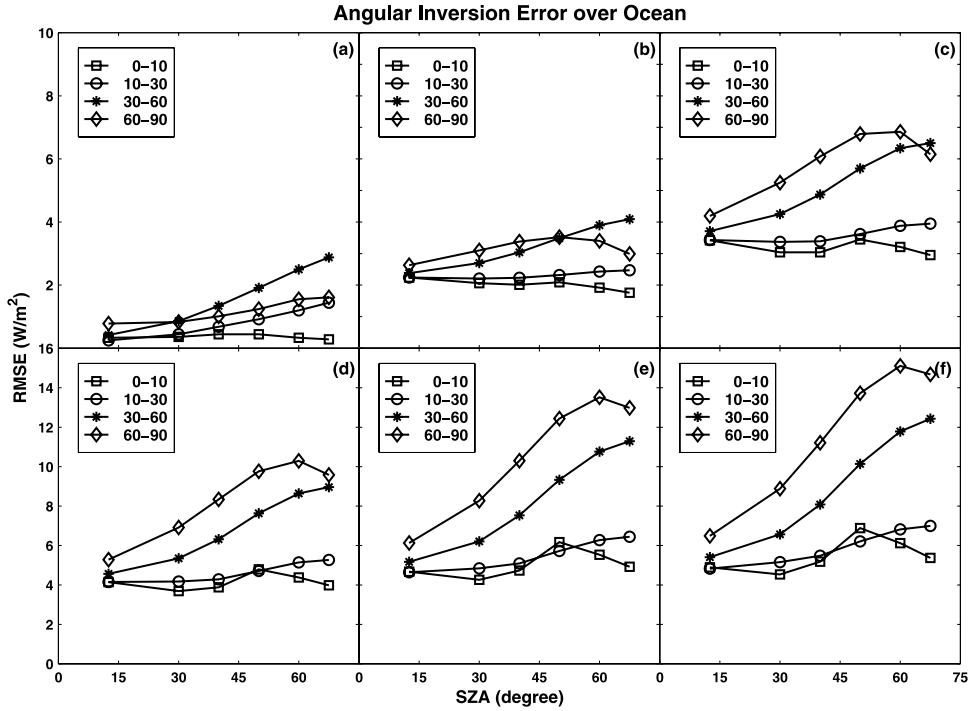

Figure 12. Shortwave RMSE versus SZA for ocean, computed with method 6 and VZA = ±55°. (a) to (f) correspond to increasing cloud cover interval. The legend shows different relative azimuth intervals.

taking all the RMSEs into account will depend on the selected orbit, as has already been shown above.

5.2. LW Band

[51] A parallel work has been developed in the longwave part of the spectrum with the along-track methodology, as in the previous section when using the single-view methodology. In this case, a viewing zenith angle of ±55° was selected a priori to make SW and LW measurements compatible, although from a theoretical point of view, this might not be the best option for LW, if Figure 8 is taken into account. However, the results would not significantly differ if this angle were modified by only a few degrees.

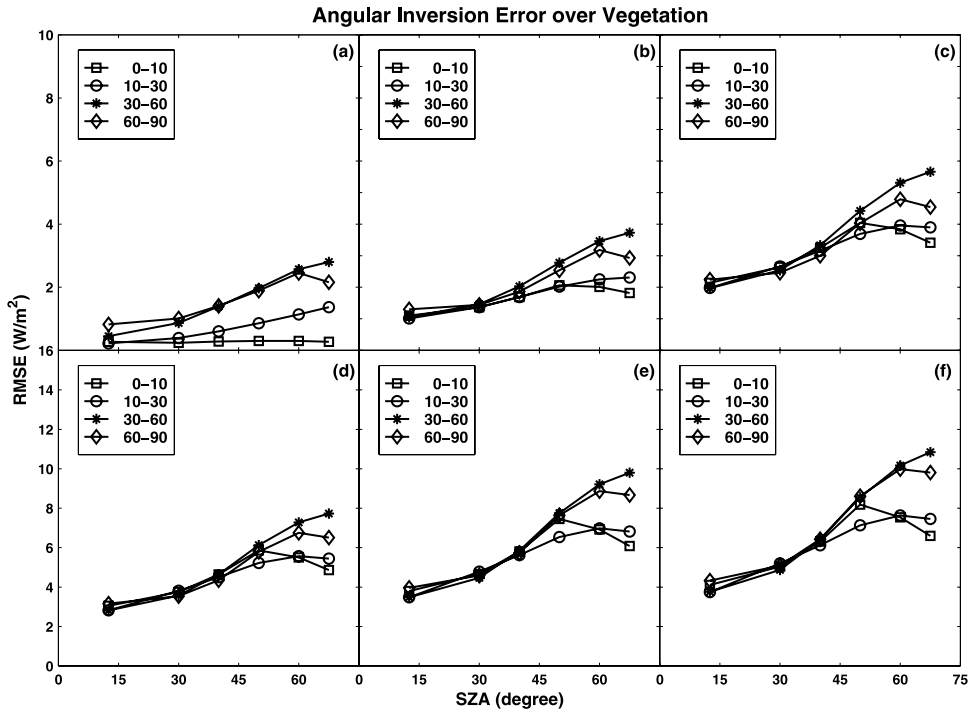

Figure 13. Same as Figure 12, but for vegetation.

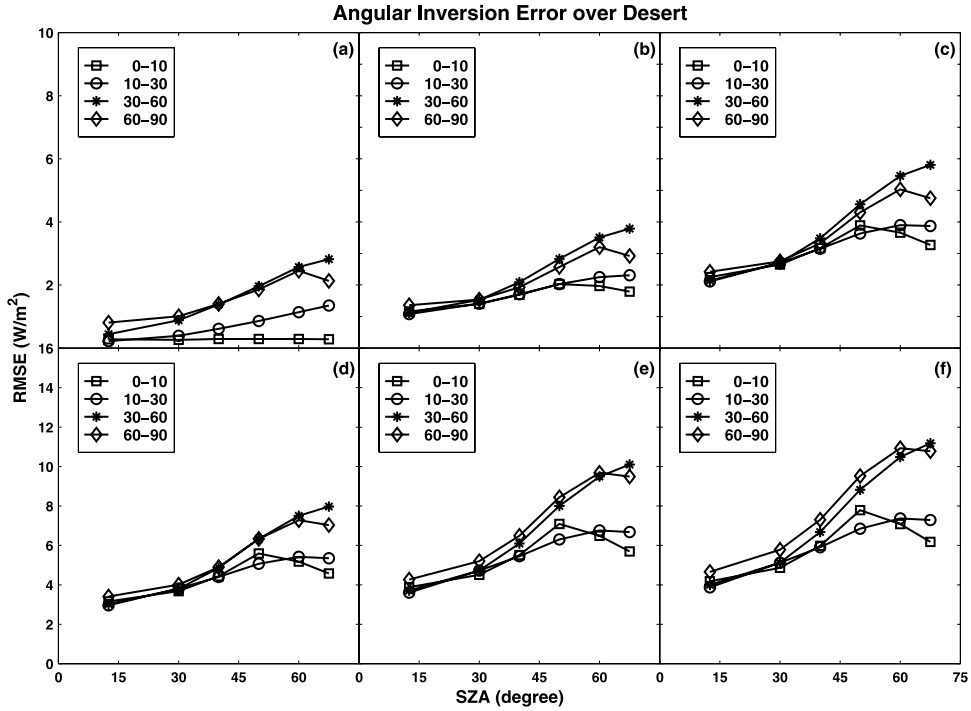

Figure 14. Same as Figure 12, but for desert.

[52] Figure 15 shows the RMSE error over ocean as obtained by using method 6, as a function of the cloud cover index, from 1 (clear sky) to 6 (overcast). As we can see, the error also increases with cloud cover, but the absolute values are always below 1 W/m^2, which is almost an order of magnitude lower than the analogous results in shortwave, shown in Figure 12. This implies that a design concept of an along-track broadband radiometer should be mainly focused on the optimization of the configuration of the SW channel, due to the fact that anisotropy of the LW radiance field is much lower and, therefore, the retrieval error is also lower.

6. Conclusions

[53] A study of the advantages of an along-track radiometer to measure TOA fluxes, both in longwave and shortwave has been carried out. A database of radiance fields was previously generated using a plane-parallel radiative transfer code. These radiance fields were obtained for different atmospheric conditions in order to simulate a wide range of realistic situations. Then, different angular distribution models were constructed to study the impact of the VZA on the flux retrieval error. This study was carried out using different design concepts such as single- and multiple-view (along-track) approaches.

[54] Although the study was carried out for different representative surfaces, the results analyzed here mainly correspond to those obtained for ocean. The reason is that results over ocean represent the worst case, and the main conclusions do not change significantly for the rest of surfaces. In addition, our main interest is to study the inversion process under mostly cloudy or overcast conditions, where the main signal comes from the cloud layer and not from the surface.

[55] Different parallel studies on angular sampling were developed, with single- and multiple-view approaches, one for SW and another for LW. These showed that there are two regions of preferable observation angles. These regions are located close to 55°–60° viewing zenith angles, both in forward and backward scattering direction in SW band, and close to 50° in LW. These results agree with those of *Davies* [1984]. The information provided by an along-track sensor with three views, namely one nadir and two off-nadir angles

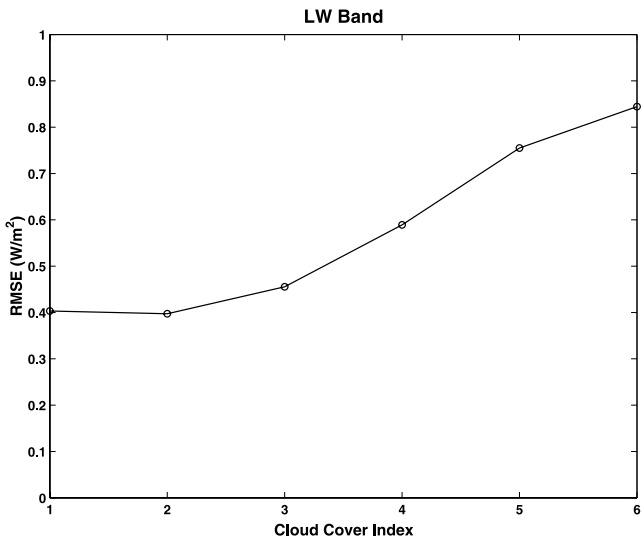

Figure 15. Behavior of the LW RMSE as a function of cloud cover over ocean. Method 6 was employed to build the ADM. Indices from 1 to 6 correspond to cloud cover intervals [0–1, 1–25, 25–50, 50–75, 75–99, 99–100], respectively.

at ±55°, has shown that the RMSE of the SW flux retrieval algorithm is lower than 10 W/m^2 in most cases. It may be improved either by optimizing the orbit, or by increasing the complexity of the inversion model.

[56] All of these results have been obtained assuming constant pixel size and perfect coregistration of the along-track views at the reference level. If these two problems are adequately addressed in a real sensor, an along-track design concept seems to be the best option to measure instantaneous TOA fluxes with high accuracy. Although this type of nonscanner along-track configurations do not provide global spatial coverage, they can be very powerful complements as boundary conditions for atmospheric profile measurements consisting of downward looking active instruments, like radar and lidar.

[57] **Acknowledgments.** The authors wish to thank P. Baptista, B. Kandel, W. Leibrandt, R. Mercier, X. Bozec, and J. L. Bezy for their helpful comments and criticisms. This work was funded by ESA contract ESTEC 14685/00/NL/JSC. It was also partially funded by the project SCALES under Programa Nacional de Espacio contract ESP2002-03678. One of the authors, A. Bodas, holds a predoctoral grant funded by Conselleria de Educació i Cultura de la Generalitat Valenciana.

References

Barkstrom, B. R., and G. L. Smith, The Earth Radiation Budget Experiment: Science and implementation, *Rev. Geophys.*, *24*, 379–390, 1986.

Barkstrom, B. R., E. F. Harrison, G. L. Smith, and R. D. Cess, Results from the Earth Radiation Budget Experiment (ERBE), *Adv. Space Res.*, *9*, 75–82, 1989.

Briegleb, B. P., P. Minnis, V. Ramanathan, and E. Harrison, Comparison of regional clear-sky albedos inferred from satellite observations and model computations, *J. Clim. Appl. Meteorol.*, *25*, 214–226, 1986.

Davies, R., Reflected solar radiances from broken cloud scenes and the interpretation of scanner measurements, *J. Geophys. Res.*, *89*, 1259–1266, 1984.

Duvel, J.-P., M. Viollier, P. Raberanto, R. Kandel, M. Haeffelin, L. A. Pakhomov, V. A. Golovko, J. Mueller, R. Stuhlmann, and the ISSWG, The ScaRaB-Resurs Earth Radiation Budget dataset and first results, *Bull. Am. Meteorol. Soc.*, *82*, 1397–1408, 2001.

European Space Agency, The five candidate Earth Explorer Core Missions EarthCARE Earth Clouds, Aerosols, and Radiation Explorer, *ESA SP-1257(1)*, Paris, 2001.

Fu, Q., and K. N. Liou, Parameterization of the radiative properties of cirrus clouds, *J. Atmos. Sci.*, *50*, 2008–2025, 1993.

House, F. B., A. Gruber, G. E. Hunt, and A. T. Mecherikunnel, History of satellite missions and measurements of the Earth radiation budget (1957–1984), *Rev. Geophys.*, *24*, 357–377, 1986.

Hu, Y. X., and K. Stamnes, An accurate parameterization of the radiative properties of water clouds suitable for use in climate models, *J. Clim.*, *6*, 728–742, 1993.

Hunt, G. E., R. Kandel, and A. T. Mecherikunnel, A history of presatellite investigations of the Earth's radiation budget, *Rev. Geophys.*, *24*, 351–356, 1986.

Jacobowitz, H., H. V. Soule, H. L. Kyle, F. B. House, and NIMBUS 7 ERB Experiment Team, The Earth Radiation Budget (ERB) Experiment: An overview, *J. Geophys. Res.*, *89*, 5021–5038, 1984.

Kandel, R., M. Viollier, P. Raberanto, J. P. Duvel, L. A. Pakhomov, V. A. Golovko, A. P. Trishchenko, J. Mueller, E. Raschke, R. Stuhlmann, and the International ScaRaB Scientific Working, The ScaRaB Earth Radiation Budget dataset, *Bull. Am. Meteorol. Soc.*, *79*, 765–783, 1998.

Key, J., Streamer User's Guide, *Tech. Rep. 96-01*, 90 pp., Dep. of Geogr., Boston Univ., Boston, Mass., 1998.

Lee, R. B., III, et al., Prelaunch calibrations of the Clouds and the Earth's Radiant Energy System (CERES) tropical rainfall measuring mission and Earth Observing System Morning (EOS-AM1) spacecraft thermistor bolometer sensors, *IEEE Trans. Geosci. Remote Sens.*, *36*, 1173–1185, 1998.

Loeb, N. G., K. J. Priestley, D. P. Kratz, E. B. Geier, R. N. Green, B. A. Wielicki, P. O'Rawe Hinton, and S. K. Nolan, Determination of unfiltered radiances from the clouds and the Earths radiant energy system instrument, *J. Appl. Meteorol.*, *40*, 822–835, 2001.

Minnis, P., and M. M. Khaiyer, Anisotropy of land surface skin temperature derived from satellite data, *J. Appl. Meteorol.*, *39*, 1117–1129, 2000.

Nakajima, T., and M. Tanaka, Algorithms for radiative intensity calculations in moderately thick atmospheres using a truncation approximation, *J. Quant. Spectrosc. Radiat. Transfer*, *40*, 51–69, 1988.

Ramanathan, V., R. D. Cess, E. F. Harrison, P. Minnis, B. R. Barkstrom, E. Ahmad, and D. Hartmann, Cloud-radiative forcing and climate: Results from the Earth Radiation Budget Experiment, *Science*, *243*, 57–63, 1989.

Raschke, E., T. H. Vonder Haar, W. R. Bandeen, and M. Pasternak, The annual radiation balance of the Earth-Atmosphere System during 1969–70 from Nimbus 3 measurements, *J. Atmos. Sci.*, *30*, 341–364, 1973.

Rossow, W. B., and R. A. Schiffer, ISCCP Cloud Data Products, *Bull. Am. Meteorol. Soc.*, *72*, 2–20, 1991.

Rossow, W. B., and R. A. Schiffer, Advances in understanding clouds from ISCCP, *Bull. Am. Meteorol. Soc.*, *80*, 2261–2287, 1999.

Shettle, E. P., and R. W. Fenn, Models for the aerosols of the lower atmosphere and the effects of humidity variations on their optical properties, *Environ. Res. Pap. 676, AFGL-TR-79-0214*, 94 pp., Air Force Geophys. Lab., Hanscom Air Force Base, Mass., 1979.

Smith, G. L., and N. Manalo-Smith, Scene identification error probabilities for evaluating Earth radiation measurements, *J. Geophys. Res.*, *100*, 16,377–16,385, 1995.

Smith, G. L., R. N. Green, E. Raschke, L. M. Avis, J. T. Suttles, B. A. Wielicki, and R. Davies, Inversion methods for satellite studies of the Earth's radiation budget: Development of algorithms for the ERBE mission, *Rev. Geophys.*, *24*, 407–421, 1986.

Smith, G. L., N. Manalo-Smith, and L. M. Avis, Limb-darkening models from along-track operation of the ERBE scanning radiometer, *J. Appl. Meteorol.*, *33*, 74–84, 1994.

Stamnes, K., S. C. Tsay, W. Wiscombe, and K. Jayaweera, Numerically stable algorithm for discrete ordinate-method radiative transfer in multiple scattering and emitting layered media, *Appl. Opt.*, *27*, 2502–2509, 1988.

Suomi, N. E., The Thermal Radiation Balances Experiment onboard Explorer 7, *NASA Tech. Note*, *D608*(11), 273–305, 1961.

Suttles, J. T., R. N. Green, P. Minnis, G. L. Smith, W. F. Staylor, B. A. Wielicki, I. J. Walker, D. F. Young, V. R. Taylor, and L. L. Stowe, *Angular Radiation Models for Earth-Atmosphere System,* vol. I, *Shortwave Radiation*, NASA, Greenbelt, Md., 1988.

Suttles, J. T., R. N. Green, G. L. Smith, B. A. Wielicki, I. J. Walker, V. R. Taylor, and L. L. Stowe, *Angular Radiation Models for Earth-Atmosphere System*, vol. II, *Longwave Radiation*, NASA, Greenbelt, Md., 1989.

Tanré, D., C. Deroo, P. Duhaut, M. Herman, J. J. Morcrette, J. Perbos, and P. Y. Deschamps, Simulation of the satellite signal in the solar spectrum (5S), report, 262 pp., Lab. d'Optique Atmos., Villeneuve d'Ascq, France, 1986.

Taylor, V. R., and L. L. Stowe, Reflectance characteristics of uniform Earth and cloud surfaces derived from NIMBUS 7 ERB, *J. Geophys. Res.*, *89*, 4987–4996, 1984.

Wielicki, B. A., B. R. Barkstrom, E. F. Harrison, R. B. Lee III, G. L. Smith, and J. E. Cooper, Clouds and the Earth's Radiant Energy System (CERES): An Earth observing system experiment, *Bull. Am. Meteorol. Soc.*, *77*, 853–868, 1996.

Wielicki, B. A., et al., Evidence for large decadal variability in the tropical mean tadiative rnergy budget, *Science*, *295*, 841–844, 2002.

Wiscombe, W. J., and J. W. Evans, Exponential-sum fitting of radiative transmission functions, *J. Comp. Phys.*, *24*, 416–444, 1977.

A. Bodas-Salcedo, J. F. Gimeno-Ferrer, and E. López-Baeza, Departamento de Termodinámica, Facultad de Física, Universidad de Valencia., C/Doctor Moliner, 50., 46100 Burjassot, Spain. (Alejandro.Bodas@uv.es; Jaume.F.Gimeno@uv.es; Ernesto.Lopez@uv.es)